A Standard Process for the Design of a High-Powered Amateur Solid Rocket Motor

Owen H. Pollack*, Tomas L. Salvo*, Jacob W. Buell*, and Andrew G. Shi†
Georgia Institute of Technology, Atlanta, Georgia, 30332

As a way to introduce students to the principles of propulsion and solid rocket motor (SRM) design, Georgia Tech Experimental Rocketry (GTXR), a subdivision of the Ramblin' Rocket Club at Georgia Tech, organizes an annual new-student high-powered solid rocket motor development program. This paper discusses the simulation models, analysis techniques, and design decisions involved in the development of one such SRM. A computer program was developed based on combustion and compressible flow theory to evaluate the theoretical motor performance with provided dimensions and constants. This program is capable of simulating both BATES and star grain propellant geometries, allowing for the selection of an optimal propellant grain geometry given various design constraints and performance targets. Commercial design software was then used to produce initial concepts of motor assemblies. Concepts were evaluated using finite element analysis (FEA) and computational fluid dynamics (CFD) software to ensure sufficient factors of safety. The iteration of motor design was informed by these results, enabling the optimization of performance metrics such as mass ratios and factors of safety. The comprehensive simulation modeling, along with mechanical and fluid analysis, resulted in an innovative high-power amateur SRM concept with confident safety margins and manufacturability.

I. Nomenclature

A^*	=	throat area	T_0	=	stagnation temperature	r_i	=	inner radius
A_b	=	burn surface area	a	=	burn rate coefficient	r_o	=	outer radius
A_e	=	grain end surface area	c^*	=	characteristic velocity	r_p	=	star point radius
A_p	=	grain port surface area	e	=	star grain angular fraction	w	=	star grain web distance
L_g	=	grain length	f	=	star grain fillet radius	y	=	burn distance
M	=	mach number	$\dot{m}$	=	mass flow	θ	=	star grain opening angle
N_g	=	number of grains	n	=	pressure exponent	γ	=	specific heat ratio
P_c	=	chamber pressure	n^*	=	number of star points	ρ	=	propellant solid density
R	=	specific gas constant	$\dot{r}$	=	burn rate			

II. Introduction

At Georgia Tech, one of the largest student engineering teams on campus is Georgia Tech Experimental Rocketry (GTXR), a subdivision of the Ramblin' Rocket Club student organization. The main mission of GTXR is to become the first collegiate rocket team to reach space using a two-stage rocket. As commercially-produced solid rocket motors (SRM) currently in production possess insufficient impulse for a two-state space-shot rocket, GTXR's Propulsion subteam develops and manufactures custom motors in-house. Due to the nature of being a collegiate engineering team, most new members who join every year are first- or second-year undergraduate students who have had little to no experience in the subject of rocket propulsion. Therefore, as a comprehensive introduction to propulsion, GTXR organizes a high-powered solid rocket motor development program anually where teams of new members are guided in the process of simulating, designing, and manufacturing a SRM from scratch. This paper documents the process used for the development of one such SRM in the hope that it may be useful to those beginning their journey into solid rocket propulsion.

*Undergraduate Members, Georgia Tech Experimental Rocketry, Daniel Guggenheim School of Aerospace Engineering, AIAA Student Members. Primary Authors.

†Undergraduate Advisor, Georgia Tech Experimental Rocketry, Daniel Guggenheim School of Aerospace Engineering, AIAA Student Member.

III. Simulation

A. Background

To understand and simulate theoretical motor performance, a quantitative understanding of the fundamental principles that govern the burning of solid propellant needs to be established.

The process begins with selecting a propellant formulation. It is assumed that the characteristics of the propellant are known prior to the start of the motor design process, including its solid density (ρ), characteristic velocity ($c*$), stagnation temperature (T_0), specific gas constant (R), and specific heat ratio (γ). Publicly available propellant evaluation programs (PEP) can be used to calculate these constants.

Next, the iterative simulation values are calculated. Chamber pressure can be found as:

$$P_c = (K_n c^* a \rho)^{1/1-n}, \tag{1}$$

where K_n, the ratio between the burn surface area (A_b) and throat area ($A*$) [1]. The chamber pressure is a critical factor to consider for the safety of the motor design, influencing the materials and retention methods selected. St. Robert's law is used to determine the burn rate ($\dot{r}$) and can be calculated as:

$$\dot{r} = a P_c^n, \tag{2}$$

where a and n are the burn rate coefficient and the pressure exponent, respectively [1]. These values are unique to every propellant formulation and must be empirically determined. Note that the surface area burns and progresses normal to the surface. This is particularly relevant a star-shaped grain geometry, as sharp points will naturally evolve into curves.

The last formula specific to solid propellant burning is for mass flow. Mass flow can be determined using the equation:

$$\dot{m} = \rho A_b \dot{r}. \tag{3}$$

It is important to recognize that these equations are intertwined; the increased burn surface area raises chamber pressure, which in turn raises the burn rate, raising the mass flow. These relationships allow for many different thrust curves to be created, impacting motor performance by tweaking the initial conditions and constants.

With these equations, attention can be turned towards the geometry of the propellant itself. In SRMs, the propellant is cast into grains that are loaded into the motor hardware. Many different grain geometries can be used, resulting in different thrust curves from the evolution of the burn area over the course of the burn. Fig. 1 demonstrates the relatively linear relationship between surface area and thrust.

This paper will examine two types of grain geometries: BATES and star. The BATES grain geometry consists only of cylindrical grains with a concentric cylindrical hole, or port, through the center of the grain (Fig. 2). It is the most common grain in amateur rocketry due to its ease of manufacturing and simulation. The star grain is a more complex geometry, but allows for a thrust curve to be more precisely customized due to the increased geometric flexibility of a star shape. Star grain geometries can result in a range of thrust curves, from neutral (flat) thrust curves to progressive and regressive curves. When using a star grain geometry, there are two main categories of star shapes: pointed stars and filleted stars (Fig. 3).

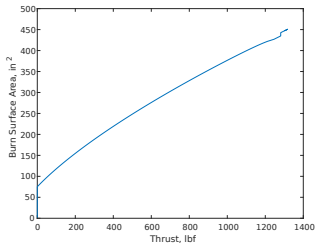

Fig. 1 Burn surface area vs. thrust for a sample star grain.

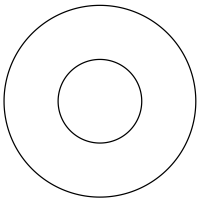

Fig. 2 A cross-section of a sample BATES Grain.

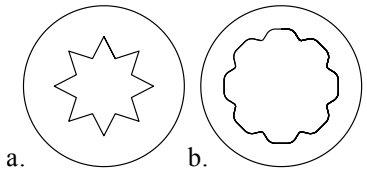

Fig. 3 (a) A cross-section of a pointed star grain. (b) A cross-section of a filleted star grain.

At its core, SRM simulation is a geometry problem. Though all performance variables, such as pressure and thrust, evolve throughout the burn, they are fundamentally functions of the burn surface area. This means that if the surface area can be calculated, all remaining values can then be determined through their respective equations. The propellant

burns in two ways: port burning and end burning. Port burning is the burning that occurs along the interior port surface of the grain, burning outwards towards the casing. The second is end burning, the axial burning on the top and bottom surfaces of the grain in towards its center. In most cases, grains are significantly longer than they are wide (their axial length is larger than their diameters), meaning grains usually burn through its entire web (the distance between the outer diameter of the grain and the largest diameter point of the interior geometry) before the ends burn to the center.

B. BATES Geometries

The initial port surface area can be calculated using:

$$A_p = (2\pi r_i)L_g. \tag{4}$$

As the end surface area is just a washer, the grain end surface area can be calculated as:

$$A_e = 2(\pi r_o^2 - \pi r_i^2). \tag{5}$$

If the ends of grains are inhibited (prevented from burning), Eq.(5) can be omitted from the overall burn area calculation.

The overall burn surface area is calculated by summing the port and end surface areas of every grain. To calculate the surface area as the burn progresses, the radius of the inner circle grows while the length of the grain shrinks proportional to the distance burned, y. Thus:

$$A_b = (2\pi(r_i + y))N_g(L_g - 2y) + 2(\pi r_o^2 - \pi(r_i + y)^2). \tag{6}$$

The burn area is repeatedly calculated for every time step throughout the simulation duration.

C. Star Grain Geometries

These equations and derivations expand on methods previously established for calculating the burn surface area of star grains in Refs. [2, 3]. The star is defined using five initial values: the number of star points (n^*), the fillet radius (f), the angular fraction (e), the web distance (w), and the opening angle (θ).

For a filleted star, the angular fraction is used to determine where the fillet begins (Fig. 4). In the case where a pointed star is desired, the fillet and angular fraction are set to 0 and 1 respectively. To simplify calculations, the symmetry of the star can be used. It is only necessary to examine half of one of the star points (Fig. 5), after which the values found can be multiplied by $2n^*$.

The burn progression of the star grain is more complex than that of the BATES grain and must first be divided into two types of progressions: the first is the scenario where the star leg will burn through before the web, and the second occurs when there is a shallower opening angle or a short web, causing the web to burn through prior to the leg (Fig. 6). The second scenario introduces certain simplifications and will be discussed after the equations for the first scenario have been established.

The overall progression for the geometry where the leg burns through can also be separated into three distinct phases: the first phase lasts from the initial burn up to the point where the star leg disappears, the second phase then progresses until the web burns through, at which point the third phase begins and the grain is reduced to sliver burning. To calculate the port surface area, the perimeter can be calculated along three edges: the leg (S_1), the curve that evolves either from the initial fillet or the sharp point (S_2), and in the case that there is a fillet, the line between the start of the fillet and the edge of the star section (S_3) (Fig. 7).

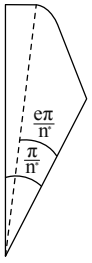

Fig. 4 The angle derived from the angular fraction, governing the start of the fillet.

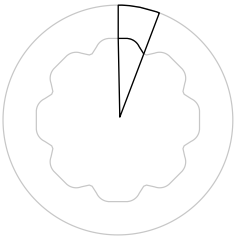

Fig. 5 The portion of the grain analyzed to simplify calculations through symmetry.

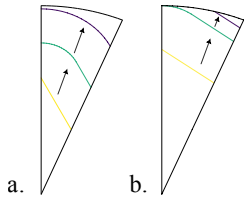

Fig. 6 (a) The burn progression for a geometry where the leg burns through. (b) The burn progression for a geometry where the leg remains.

S_1 can first be determined for the initial case where there is no fillet. Application of trigonometric relations shows that:

$$S_1 = (r_p \sin(e\pi/n^*))/\sin(\theta/2). \tag{7}$$

For when there is a fillet or the burn has progressed, a second term must be added which will shorten the total length:

$$S_1 = (r_p \sin(e\pi/n^*))/\sin(\theta/2) - ((f + y)\cot(\theta/2)). \tag{8}$$

Next S_2 is found. As it is a slice of a circle with radius f that will grow with y, first the angle must be found:

$$\omega = (\pi/2) - (\theta/2) + (e\pi/n^*), \tag{9}$$

$$\therefore S_2 = (f + y)\omega. \tag{10}$$

Finally, using the arc length formula, S_3 can be determined as:

$$S_3 = (r_p + f + y)((\pi/n^*) - (e\pi/n^*)). \tag{11}$$

Accounting for the expansion due to symmetry gives a total port surface area of:

$$A_p = 2n^* N_g L_g (S_1 + S_2 + S_3). \tag{12}$$

To find the end surface area, the star section can be further divided into four sections (Fig. 8). As the first section is a slice of a circle with an angle derived from the angular fraction, it will have a section area of:

$$A_{e_1} = (1/2)((\pi/n^*) - (e\pi/n^*))(r_p + f + y)^2. \tag{13}$$

Next, the second section area is a slice of the circle with radius f that grows with y along the same angle ω previously found (Eq. 9), so its area is:

$$A_{e_2} = (1/2)(f + y)^2\omega. \tag{14}$$

The third section is a right-angle trapezoid, so to use the formula for the area of a trapezoid, its bases and heights must first be determined. The height is $(f + y)$ and one base can be seen to be S_1. The other base, as shown in Fig. 9, can be simplified to:

$$B_2 = S_1 + (\cot(\theta/2)(f + y)), \tag{15}$$

$$\therefore A_{e_3} = ((S_1 + B_2)(f + y))/2. \tag{16}$$

The last area is a triangle with known legs of r_p and B_2. The angle between them can be derived as:

$$\alpha = \pi - (\pi - (\theta/2)) - (e\pi/n^*) = (\theta/2) - (e\pi/n^*), \tag{17}$$

$$\therefore A_{e_4} = (1/2)B_2 r_p \sin(\alpha). \tag{18}$$

This gives a final end area of:

$$A_e = 2(\pi r_o^2 - (A_{e_1} + A_{e_2} + A_{e_3} + A_{e_4})). \tag{19}$$

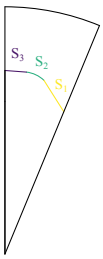

Fig. 7 The three side lengths of the port surface perimeter.

Fig. 8 The four sections that the total area is divided into during the first phase.

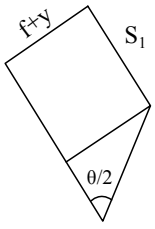

Fig. 9 The side length and angles necessary to find the area of the trapezoid.

As this phase lasts until the star leg S_1 burns through, the condition for this phase can be seen to be:

$$S_1 \geq 0. \tag{20}$$

Moving to phase two, since S_1 has burned through, only S_2 and S_3 need to be calculated. S_2 can still be calculated as an arc length, however, the angle changes as the end point of the arc moves up along the line of symmetry. Using the previously obtained angles and values, the angle and therefore S_2 can be calculated as:

$$\phi = (\pi/2) + (e\pi/n^*) - \tan^{-1}\left(\sqrt{(f+y)^2 + (r_p \sin(e\pi/n^*))^2}/(r_p \sin(e\pi/n^*))\right), \tag{21}$$

$$\therefore S_2 = (f+y)\phi. \tag{22}$$

Since S_3 will be governed by the previously derived equation (Eq. 11) until the web burns through, the total port surface area is:

$$A_p = 2n^* N_g L_g (S_2 + S_3). \tag{23}$$

The end area can again be divided into four sections (Fig. 10). The first section can be calculated as a slice of a circle as the radius and angle are already known:

$$A_{e_1} = (1/2)((\pi/n^*) - (e\pi/n^*))(r_p + f + y)^2. \tag{24}$$

The second section is a right triangle with a known height of $r_p \sin(e\pi/n^*)$ so the area can be calculated as:

$$A_{e_2} = (1/2)(r_p \sin(e\pi/n^*))((r_p \sin(e\pi/n^*)) \cot(e\pi/n^*)). \tag{25}$$

The third area is another right triangle with a first base $r_p \sin(e\pi/n^*)$ whose other base can be found using the Pythagorean theorem, giving an area of:

$$A_{e_3} = (1/2)(r_p \sin(e\pi/n^*))\sqrt{(f+y)^2 - (r_p \sin(e\pi/n^*))^2}. \tag{26}$$

The last area is another slice of a circle, in this case with a radius of $(f+y)$ at the angle ϕ calculated for S_2 (Eq. 21):

$$A_{e_4} = (1/2)\phi(f+y)^2. \tag{27}$$

$$\therefore A_e = 2(\pi r_o^2 - (A_{e_1} + A_{e_2} + A_{e_3} + A_{e_4})). \tag{28}$$

As this phase progresses until the web has burned through, its condition is $y \leq w$. For the final phase, there is just sliver burning. This means that the port surface area will be an arc length calculation, but first, the angle must be found. Using trigonometry (Fig. 11), the overall angle from the start of the fillet can be calculated as:

$$\beta = (\pi/2) - (\theta/2) + (e\pi/n^*). \tag{29}$$

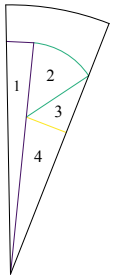

Fig. 10 The four sections that the total area is divided into during the second phase.

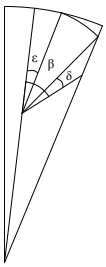

Fig. 11 The angles governing where the arc begins and ends relative to its original angle.

To find the angle over which the arc length is not exceeding the outer diameter or edge of the star-section, two more angles must be derived (Fig. 11):

$$\delta = \tan^{-1}\left(\sqrt{(f+y)^2 - (r_p \sin(e\pi/n^*))^2}/(r_p \sin(e\pi/n^*))\right) - (\theta/2), \tag{30}$$

$$\varepsilon = \pi - \cos^{-1}\left(-\left((r_o)^2 - (r_p)^2 - (f+y)^2\right)/(2r_p \sin(f+y))\right), \tag{31}$$

$$\therefore A_p = 2n^* N_g L_g\big((f+y)(\beta - \delta - \varepsilon)\big). \tag{32}$$

For the end area during sliver burning, previous works either omit the area as final losses or approximate the area with an equation that will cause a discontinuity during the switch from the second to third burn phase. To avoid this, a linear approximation was used to assume that during the brief sliver burning, the end area progresses linearly to zero. While this approach is not exact, it lowers the error margin to provide a more realistic result of the overall burn, particularly during this final phase. This is a key point of improvement for this model moving forward. This linear approximation is calculated with the max burn distance, intercept, and slope:

$$y_{\max} = \sqrt{(r_o - r_p \cos(e\pi/n^*))^2 + (r_p \sin(e\pi/n^*))^2} - f, \tag{33}$$

$$i = (\pi r_o^2) - (m y_{\max}), \tag{34}$$

Let $h = r_p \sin(e\pi/n^*)$, then:

$$m = \frac{\left(\pi r_o^2 - n^*\left((\pi/2) + (e\pi/n^*) - \tan^{-1}(\sqrt{(f+w)^2 - h^2}/h))(f+w)^2 + (\cot(e\pi/n^*))h^2 + h\sqrt{(f+w)^2 - h^2} + (r_p + f + w)^2((\pi/n^*) - (e\pi/n^*)\right)\right)}{(y_{\max} - w)}, \tag{35}$$

$$\therefore A_e = (my) + i. \tag{36}$$

Now that the burn progression for a typical star is established, the second scenario presented in Fig. 6 can be addressed. Here, the entire burn consists only of the previously defined first and third phases as S_1 remains until the burn is finished. Both the port and end surface areas can be calculated as before for the first phase. For the final phase, since the web has burned through, S_3 will not be present, so only S_1 and S_2 need to be defined. To calculate S_1, a series of angles and lengths must be derived:

$$\mu = (e\pi/n^*) + (\pi/2) - \beta, \tag{37}$$

$$\zeta = \sqrt{(r_p \sin(e\pi/n^*))^2 + y^2 - 2y(r_p \sin(e\pi/n^*))\cos(\mu)}, \tag{38}$$

$$\kappa = (\pi/2) - \left(\sin^{-1}(y \sin(\mu))/\zeta\right), \tag{39}$$

$$\therefore S_1 = (\zeta \sin(\kappa))/(\pi - (\theta/2)). \tag{40}$$

The calculation for S_2 during the final phase is almost the same as before; though, the angle δ is unnecessary, therefore:

$$S_2 = (f+y)(\beta - \varepsilon), \tag{41}$$

$$\therefore A_p = 2n^* N_g L_g (S_1 + S_2). \tag{42}$$

To find the end area of the remaining sliver, a similar approximation is used as before. In this case, however, since S_1 is a straight line, the area can be better approximated as a triangle, where the height is:

$$h_t = r_o - (y \csc(\theta/2)) - \left((r_p \sin((\theta/2) - (e\pi/n^*)))/\sin(\pi - (\theta/2))\right), \tag{43}$$

$$A_t = (1/2)h_t\sqrt{(S_1 + S_2)^2 - h_t^2}, \tag{44}$$

$$\therefore A_e = \pi r_o^2 - 2n^* A_t. \tag{45}$$

D. Simulation Output Calculations

With the burn surface area expressions, the motor performance values can be found. Flow conditions through the nozzle are assumed to be isentropic [1], allowing isentropic relations to be used to find the Mach number of the flow, the optimal nozzle exit diameter, the exit exhaust pressure, and the exit temperature. Readers are directed to Ref. [1] for the derivations of these values. The exit velocity of the flow follows as:

$$v = M\sqrt{\gamma R T_{\text{exit}}}. \tag{46}$$

Thrust can then be calculated as:

$$F_t = \dot{m}v + A_{\text{exit}}(P_{\text{exit}} - P_{\text{atmospheric}}). \tag{47}$$

Lastly, total impulse can be found by numerically integrating thrust with respect to time.

The prior burn area and motor performance equations were implemented into a MATLAB program that looped through iterations of the motor state as the burn progresses. The results of the pointed stars were then successfully validated against other commercial off-the-shelf (COTS) simulations. Then, as there is no publicly available program that simulates filleted stars, sample grains were created in SolidWorks, a computer-aided design (CAD) software. The port and end areas could then be found using the evaluation tools in SolidWorks. This was done at multiple points during the burn and in different phases of the burn. Analysis performed for various different grain geometries across all main burning scenarios agreed with the MATLAB simulation model. A sample of the grain recreations and analysis in SolidWorks can be seen in Fig. 12.

Fig. 12 A sample of the area calculations performed in SolidWorks. Note, the third image only measures the 1/8th of the total area.

E. Grain Selection

For the motor designed in this paper, a star grain geometry was selected to experiment with achieving a flat thrust curve. As the nozzle can only be optimized for a single pressure value, achieving a steady state pressure close to the optimal pressure value over longer durations greatly improves motor efficiency. An eight-pointed star with no fillet was used with a maximum expected operating pressure (MEOP) of 1008 psi. The total burn time was 4.504 seconds with a total impulse of 4066.5 lbf·s. The performance graphs shown in Fig. 13 illustrate the flat thrust curve that was simulated.

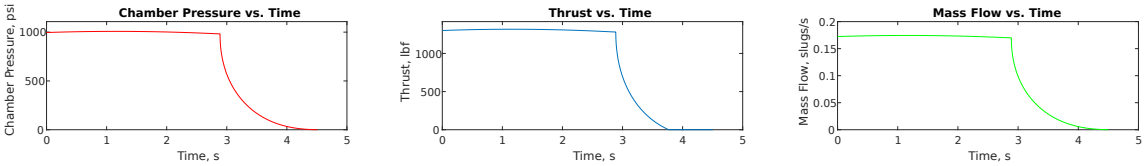

Fig. 13 The main performance graphs of the selected grain geometry.

IV. Motor Design and Analysis

The key structural components of an SRM are the motor casing, the closure retention systems, the nozzle assembly, and the igniter. The structural design of the SRM began with an understanding of the specific design constraints given by the MATLAB motor simulation. Other dimensional constraints came from the inner and outer diameter dimensions of the selected casting tubes and thermal liners. The design of the motor casing can begin with these diameter dimensions.

A. Motor Casing

The phenolic thermal liners slide into the motor casing to protect it from the heat of the combustion chamber. The selected liners had an outer diameter of 3.486 in, allowing it to fit within an motor casing with an inner diameter of 3.5 in. The motor casing must also withstand the internal pressures during the burn to avoid a casing burst or leakage. It is thus necessary to choose a material that can withstand the stress predicted by the MATLAB simulation.

Aluminum 6061-T6 was chosen as the casing material due its ease of machining, availability, and cost-effectiveness. The structural integrity of the aluminum motor casing was evaluated at MEOP in Ansys Mechanical, a commercial finite element analysis software. A fixed pressure was applied on the inside faces of the full assembly, which was connected through bonded contacts. Then, a fixed support was added to one side, producing the result shown in Fig. 14.

The maximum stress of around 9,000 psi was located on the inside of the casing tube. As aluminum 6061 has a yield strength of 40,000 psi [4], the casing factor of safety was calculated to be 4.4. A minimum safety factor of two was set as a design requirement for all parts to ensure a confident safety margin. Note that the temperature increase of the motor casing is negligible due to the low burn time and the insulation of the thermal liner. The length of the motor casing was determined by the geometry of the nozzle assembly and retention systems described in the following sections.

B. Retention Systems and Closure

The retention systems secure the forward bulkhead and nozzle assembly to the motor casing. During the burn of the motor, the chamber will experience high pressure, pushing the forward bulkhead and nozzle assembly outward. Multiple different retention methods are used in the aerospace industry, including pins, snap rings, and bolts. After careful consideration, pins were selected for their ease of installation and reliability. The pins are inserted into a ring that acts as a physical block to secure the bulkheads to the casing (Fig. 15).

A complex stress field is created around the pins as they attempt to tear through the steel casing and retention ring. Therefore, to select the number and diameter of pins to use for retention, a full forward closure simulation was conducted where the bulkhead and pin ring were allowed to slide inside the casing through the implementation of frictionless contacts (Fig. 15). A pressure of 1008 psi was applied to the inside face of the bulkhead, and a smaller mesh sizing was applied to the pins and pin holes, granting better resolution of the tear-through stresses formed. With 10 3/8-inch pins at each end of the casing, the minimum factor of safety remained above 3 for non-pin components; however, further analysis was required to validate the pins themselves.

As the pins experience a high stress state, alloy steel 4140 was selected as the pin material due to its high strength and stiffness [5]. To accurately model the stresses experienced by a pin in a shear state, the pin geometry was imported into Ansys Mechanical. Then, as shown in Fig. 16(b), two blocks were created around the pin, creating a shear line in the middle of the pin. One block was fixed while the other had a pressure force applied to it, mimicking the shear force expected by each pin. Moreover, a displacement constraint was applied to the pressure block, allowing it only to move in the shear direction. With decreased mesh sizing, the simulation (Fig. 16(a)) demonstrates that stresses are not expected to exceed 25000 psi, giving a factor of safety of 5.6.

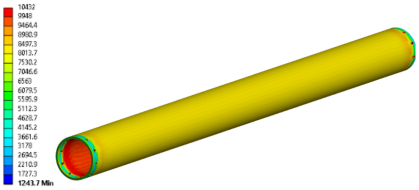

Fig. 14 Casing pressure vessel stress simulation.

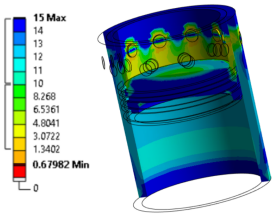

Fig. 15 Forward closure and pin ring analysis.

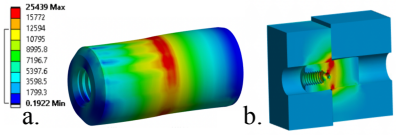

Fig. 16 Locking pin shear stress simulation.

The pin ring was designed with a thickness of 0.18 inches. In this design, there are 2 pin rings: one located in the forward closure and the other in the nozzle extension (Fig. 15). Note that the nozzle assembly pin ring is not a separate part like the forward pin ring; instead, it is embedded within the nozzle extension to reduce the number of parts involved in the nozzle assembly.

While designing the pin ring, it would have been prudent to run a bearing stress analysis. Bearing stress is the pressure caused by the contact between two objects. Consequently, it would have been preferable to create a pin with a larger width to have a greater factor of safety. As such, this analysis should be reflected in future motor designs.

C. Forward Bulkhead

The forward bulkhead holds pressure inside the casing and, as mentioned before, is retained onto the motor casing by the forward pins and pin ring. The design constraints for the forward bulkhead consist of the MEOP and the expected chamber temperature. For this SRM, stainless steel 304 was chosen for its high melting temperature and tensile strength of over 140,000 psi [5]. The width of the bulkhead was determined by structural analysis in Ansys Mechanical to achieve a FOS of above 3 (Fig. 22). The bottom face of the bulkhead has a cavity to remove unnecessary material to lower overall design mass. A fillet was added to the cavity's inner edges to reduce stress concentrations. The bulkhead analysis is shown with exaggerated deformation in Fig. 22.

D. Nozzle Assembly

The key design components of a nozzle are its converging and diverging half angle and the throat and nozzle exit diameters. The dimensions given from the MATLAB burn simulation determine the diameter dimensions for optimal flow expansion, and the half angles were selected based on previous research on ideal nozzle geometries [6]. The optimal convergence half angle is 60 degrees and the optimal divergence half angle is a range from 12-15 degrees. For this SRM, a converging half angle of 60 degrees and a diverging half angle of 13.5 degrees was chosen (Fig. 20). The throat diameter was 1.038 in. and the nozzle exit diameter was 3.100 in. (Fig. 18), selected based on the performance simulation. The nozzle can be sized according to these parameters.

There are multiple avenues for choosing how to design the nozzle, with design considerations such as temperature and stress. A three-piece nozzle assembly was chosen consisting of a graphite inner throat, which can withstand a combustion temperature 4890°R [7], assumed to be identical to the stagnation temperature of the flow and is dependent on the selected propellant. O-rings were selected using a publicly available online o-ring calculator. For this motor, o-ring dash number 152 was used for all o-rings.

Both structural and thermal analysis were necessary to validate the nozzle's safety. In Ansys mechanical, fixed supports were placed on the pinholes with friction-less contacts assigned between all bodies. The graphite was given a decreased mesh sizing as it is the focus of this simulation. As shown in Fig. 21, the pressure exerted on the nozzle creates a significant stress on the graphite insert. These stresses are concentrated at the nozzle throat and the lower o-ring grooves, allowing for a minimum safety factor of 3.2.

To validate the MATLAB grain burning simulation and provide temperature data for further thermal simulation, a fluid analysis model was set up in Ansys Fluent, a commercial CFD software. By implementing face meshing and reduced element sizings inside the nozzle, an accurate 2D axisymmetric mesh was generated. Then, a pressure inlet was assigned to the inside of the nozzle, and a pressure outlet at the plume. The realizable k-ϵ model was used for turbulence, and the Sutherland for viscosity [8].

As illustrated in Fig. 17, the simulation verifies that the nozzle is well expanded, with the exit flow pressure being similar to the atmospheric. Moreover, the model's estimated thrust of 1349 lbf supports the 1317 lbf predicted by the MATLAB simulation.

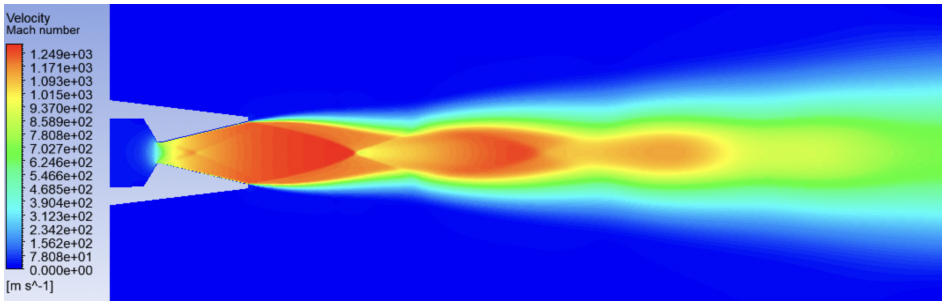

Fig. 17 CFD nozzle plume analysis.

The last component of the nozzle is the carrier for the graphite insert, which uses a stronger, less brittle, material that can better withstand the chamber pressures exerted on the assembly. Thus, stainless steel 304 was chosen due to its high melting temperature of 2500°F and its ability to withstand the stresses at MEOP with a FOS of over 3 [5]. Lastly, the carrier additionally needs to be able to interface with the graphite insert to retain the proper converging half angle.

The nozzle experiences very high heat loads during the burn; the high temperatures, coupled with the high-velocity flow lead to forced convection. Any slight deformation of the nozzle's interior surface may cause shocks to form inside,

reducing the nozzle's efficiency or even potentially causing catastrophic failure. To evaluate the ability of the nozzle components to withstand such heat loads, a transient thermal simulation model was implemented. A mesh was generated with graphite assigned to the throat insert. With a predicted stagnation temperature of 4890°R and a heat transfer coefficient of $2500 W/m^2K$ [9], a very conservative convection model was applied to the inside faces of the nozzle.

The simulation (Fig. 19) shows that the graphite insert effectively conducted heat away from the surface, cooling it enough to prevent softening or melting. The components, including o-rings, remained well below their maximum service temperatures, providing confidence for the heat resistance of the nozzle.

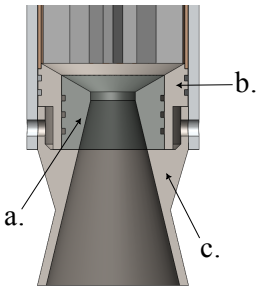

Fig. 18 The full nozzle assembly: a. The graphite insert b. The nozzle carrier c. The nozzle extension.

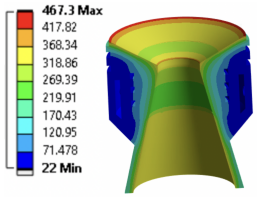

Fig. 19 Nozzle thermal analysis.

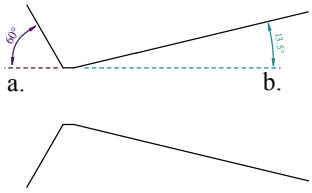

Fig. 20 a. The converging half angle b. The diverging half angle.

E. Ignitor

The final component of a SRM is the igniter, which initiates the propellant burn of the motor. There are two main types of ignition methods; head-end ignition and aft-end ignition. Aft-end ignition is simpler as the wires can be run up through the nozzle, removing most of the machining complexity and other structural considerations. However, the igniter wires must therefore be routed externally from the avionics bay of the rocket down to the nozzle, which may cause sizing issues as a larger airframe around the motor may be required. This can only be avoided by powering the igniter from a source not connected to the rocket, such as a launchpad.

Hence, head-end ignition is very beneficial for sustainer stages in multistage rockets, where external wires will likely fail due to drag forces, or if the rocket needs to be self-sufficient and able to ignite using on-board power. Thus, due to its broader use cases, head-end ignition was selected, with the igniter integrated into the forward bulkhead design. This igniter works by lighting a small propellant puck inside a chamber with 8 holes radially drilled, redirecting the flames into the star-grain cavities to ensure an even ignition. A small wire is routed through a hole into the igniter chamber that connects to the propellant. Since, the igniter is installed within the forward bulkhead, a gasket is required to maintain a proper pressure seal. Graphite was selected for the gasket, and stainless steel 304 for the igniter, both due to their ability to withstand the high chamber temperatures.

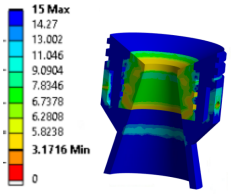

Fig. 21 3-Piece nozzle assembly structural simulation.

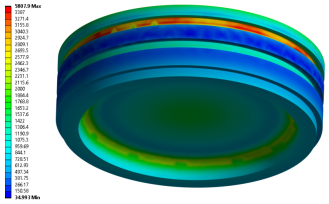

Fig. 22 Forward bulkhead analysis.

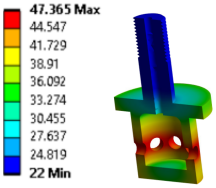

Fig. 23 Ignitor thermal analysis.

Nevertheless, if the temperature inside the chamber stays too hot for an extended period, the igniter assembly could melt and damage the propellant grains and nozzle throat. To evaluate the likelihood of this happening, a transient thermal simulation was conducted in Ansys. Convection was applied to all exposed faces of the assembly, using a surrounding temperature of 4890°R, which was predicted using isentropic relations, and a convection coefficient of $25.32 W/m^2K$ [10] . As shown in Fig. 23, the temperature of the igniter does not rise significantly during the short burn time, implying that it is very unlikely to melt.

F. Final Considerations

The final design can be seen in Fig. 24. A modified version of this motor was approved by GTXR to be funded, constructed, and static fired. The static fire will occur in late April of 2024, after which the results can be analyzed to assess the accuracy of the modeling and simulation, as well as improve on the design process established out in this paper. Additionally, the motor performance simulation remains under development to increase its accuracy and applicable use cases.

Fig. 24 The full motor assembly.

Acknowledgments

The authors would like to thank the senior members of the GTXR Propulsion subteam for their assistance and technical support throughout the motor development program.

References

[1] Sutton, G. P., and Biblarz, O., *Rocket Propulsion Elements*, 9th ed., John Wiley Sons, Inc., 2017, Chaps. 3,12.

[2] Stalin, P., Kumar, Y. N. V. S., and Nazumuddin, S. K., "Design and Geometrical Analysis of Propellant Grain Configurations of a Solid Rocket Motor," *International Journal of Engineering Development and Research*, Vol. 2, 2014, pp. 3417–3427.

[3] Barrere, M., Jaaumotte, A., de Veubeke, B. F., and Vandenkerckhove, J., *Computational Methods for Fluid Flow*, 2nd ed., Elsevier Publishing Company, Amsterdam, 1960, Chap. 6.

[4] *ASM Handbook - Properties and Selection: Nonferrous Alloys and Special Purpose Materials*, Vol. 2, ASM International, 1990. https://doi.org/10.31399/asm.hb.v02.9781627081627.

[5] Bauccio, M. L. (ed.), *ASM Metals Reference Book*, 3rd ed., ASM International, 1993.

[6] Hamedi-Estakhrsar, M. H., Mahdavy-Moghaddam, H., and Jahromi, M., "Investigation of effects of convergence and divergence half-angles on the performance of a nozzle for different operating conditions," *Journal of the Brazilian Society of Mechanical Sciences and Engineering*, Vol. 40, No. 353, 2018, pp. 1–12. https://doi.org/10.1007/s40430-018-1271-9.

[7] "Graphite Properties and Charateristics For Industrial Applications," *Entegris, Inc.*, 2020.

[8] Khan, S. A., Ibrahim, O. M., and Aabid, A., "CFD analysis of compressible flows in a convergent-divergent nozzle," *Materials Today: Proceedings*, Vol. 46, 2021, pp. 2835–2842. https://doi.org/https://doi.org/10.1016/j.matpr.2021.03.074.

[9] Mehta, R. C., "Estimation of heat-transfer coefficient in a rocket nozzle," *AIAA Journal*, Vol. 19, No. 8, 1981, pp. 1085–1086. https://doi.org/10.2514/3.7846.

[10] Yener, T., Yener, S. C., and Mutlu, R., "Convection Coefficient Estimation of Still Air Using An Infared Thermometer and Curvefitting," *Journal of Engineering Technology and Applied Sciences*, Vol. 4, No. 2, 2019, pp. 95–103. https://doi.org/10.30931/jetas.598862.